Overtones and nonlinearities in binary black hole ringdowns

Matthew Giesler[1,*] Sizheng Ma[2] Keefe Mitman[3] Naritaka Oshita[4,5,6] Saul A. Teukolsky[1,3] Michael Boyle[1]
Nils Deppe,[1,7] Lawrence E. Kidder[1] Jordan Moxon,[3] Kyle C. Nelli[3] Harald P. Pfeiffer[8] Mark A. Scheel[3]
William Throwe[1] and Nils L. Vu[3]

[1]*Cornell Center for Astrophysics and Planetary Science, Cornell University, Ithaca, New York 14853, USA*
[2]*Perimeter Institute for Theoretical Physics, Waterloo, Ontario N2L2Y5, Canada*
[3]*Theoretical Astrophysics 350-17, California Institute of Technology, Pasadena, California 91125, USA*
[4]*Center for Gravitational Physics and Quantum Information (CGPQI),*
Yukawa Institute for Theoretical Physics (YITP), Kyoto University, 606-8502, Kyoto, Japan
[5]*The Hakubi Center for Advanced Research, Kyoto University, Yoshida Ushinomiyacho,*
Sakyo-ku, Kyoto 606-8501, Japan
[6]*RIKEN iTHEMS, Wako, Saitama, 351-0198, Japan*
[7]*Department of Physics, Cornell University, Ithaca, New York 14853, USA*
[8]*Max Planck Institute for Gravitational Physics (Albert Einstein Institute),*
Am Mühlenberg 1, D-14476 Potsdam, Germany

Using high-accuracy numerical relativity waveforms, we confirm the presence of numerous overtones of the $\ell = 2$, $m = 2$ quasinormal mode early in the ringdown of binary black hole mergers. We do this by demonstrating the stability of the mode amplitudes at different fit times, ruling out the possibility that a linear superposition of modes unphysically fits a highly nonlinear part of the waveform. We also find a number of previously unidentified subdominant second-order quasinormal modes in the (2, 2) mode. Even though these modes are mathematically nonlinear, they nevertheless confirm the validity of perturbation theory as a good approximation for describing much of the ringdown.

I. INTRODUCTION

When two black holes orbit each other, they radiate energy via gravitational waves and eventually merge to form a single black hole. The gravitational waveform rises to a maximum amplitude and then settles down in a ringdown phase as the remnant black hole sheds its distortions and evolves toward a final state of equilibrium. Close enough to equilibrium, the final black hole can be approximated by linear perturbation theory of the Kerr metric [1]. In this approximation, the radiation is dominated by a set of quasinormal modes (QNMs).

The QNMs are damped oscillations of the remnant black hole, with characteristic frequencies determined by the mass and the spin of the remnant. Each QNM frequency, $\omega_{\ell mn}$, is complex valued, encoding the oscillation frequency and damping time. Here ℓ and m label the angular harmonic of a particular mode. The final index n of $\omega_{\ell mn}$ is the overtone number. It labels the eigenvalues of the radial equation for the perturbation. While the $n = 0$ mode, or fundamental mode, was typically of primary interest in ringdown studies, the overtones, $n > 0$, were often neglected and considered subdominant. Recent work [2]

challenged this notion, demonstrating that overtones are important for modeling binary black hole ringdowns and that the inclusion of overtones seems to allow for accurate modeling of the (2, 2) component of the waveform as early as its peak. This result turned out to be controversial and was met with claims of overfitting and some doubts about whether the overtones are in fact physical [3–9]. A more in-depth discussion of the connection between this previous work [2] and the current work can be found in Sec. II.

An important issue is how to distinguish a linear superposition of modes that is physical from a superposition that merely provides a good fit, that is, overfitting. A good criterion is that if the modes are really there, their amplitudes should remain constant as the start time of the fit is varied, apart from the exponential decay of each mode with its expected decay constant. Part of the reason for skepticism in the papers cited above is that they could not demonstrate that the amplitudes were constant, especially at early times and for higher overtones. We do so here.

In this paper, we investigate the presence of linear QNMs, including overtones, and second-order QNMs [10–13] in the (2, 2) component of the ringdowns of high-accuracy numerical relativity (NR) simulations. Our primary focus is a theoretical understanding of the ringdown, with a goal of determining the contributions of overtones and second-order

*Contact author: mgiesler@tapir.caltech.edu

QNMs to the ringdowns of binary black holes. We aim to determine the physical picture of the ringdown and how much of it is described by perturbation theory, either first or second order. Whether the modes we identify in this work can be detected in practice with a certain detector or sensitivity is a separate question that should be addressed in future work.

Throughout this work, we focus on two particular NR simulations from the Simulating eXtreme Spacetimes (SXS) collaboration. Both simulations are equal-mass aligned-spin binaries and both are extremely accurate. The high accuracy of these waveforms is due to improved methods in extracting the waveforms from the numerical evolutions. In particular, we use waveforms that have been extracted using a Cauchy evolution via SpECTRE's Cauchy-characteristic evolution (CCE) module [14–16]. This enables us to not only obtain much higher-accuracy waveforms, but because CCE also computes the Weyl scalars, we can map the NR system to the superrest frame of the remnant black hole [17,18] using Bondi-van der Burg-Metzner-Sachs (BMS) frame fixing [18–20]. This last step is important for removing mode-mixed QNMs that arise from being in the wrong BMS frame. If these spurious modes are not removed but left unaddressed, they effectively increase the noise floor and make fitting highly challenging. Additional details regarding the NR waveforms and preprocessing can be found in Sec. IV A.

Beyond this, an additional improvement over previous fitting techniques is the use of a much more robust nonlinear least squares algorithm called variable projection. We make use of this algorithm to perform agnostic searches for QNMs within the ringdown, identifying the best-fitting complex frequencies of unknown QNMs. For a detailed discussion of variable projection, see Sec. III B.

Identifying and extracting individual QNMs from the ringdowns of NR waveforms is a challenging task. To highlight some of the subtleties associated with fitting many modes in the presence of noise, we first treat a simplified analytic case and discuss the complications that arise. In particular, we show how sensitive the highly damped modes are to small amounts of simulated numerical noise. In Sec. IV B we introduce a technique for handling the most sensitive modes and show how this allows for better resolution of mode amplitudes as a function of time. We use this same technique in Sec. V to uncover the many QNMs in the ringdowns of our two highly accurate NR waveforms. These analyses confirm that the overtones are physical and that they can be stably extracted from binary black hole ringdowns. Moreover, we also show a number of previously unidentified second-order QNMs present in the dominant $(\ell = 2, m = 2)$ component of the ringdown. While the second-order modes are generally subdominant, they are in principle detectable, and could serve as unique probes of the nonlinear aspects of binary black hole mergers. Lastly, we explore the accuracy

of using QNMs to predict remnant parameters and discuss the connection between unmodeled nonlinearities and biased estimation. A note on our conventions: we take $c = G = 1$ and use the Moreschi-Boyle conventions of Refs. [19–25].

II. PREVIOUS WORK

In previous work [2], we explored the contribution of overtones to binary black hole ringdowns. There we showed that the inclusion of overtones provides an accurate estimate of the underlying remnant mass and spin as early as the peak[1] of the strain. Reference [2] also showed that a model with overtones provides an excellent description for the postpeak signal, with residuals comparable to the numerical error in the waveforms used in that study. Showing that amplitudes are constant up to the expected decay rates, a much stricter requirement for proving the presence of overtones, proved to be more difficult and Ref. [2] could only reliably extract up to $n = 2$ (with rough evidence for $n = 3$ and $n = 4$).

In this work, we find that with improved high-accuracy waveforms we can reliably extract the numerical decay of overtones well beyond $n = 2$. These improved waveforms, along with improved fitting techniques, yield residuals at the 10^{-8} level, whereas the prior work had numerical noise at a significantly higher level of $\sim 10^{-5}$. This lower noise floor allows us to identify previously unidentifiable modes and improves our ability to numerically extract individual modes over a much wider range of amplitudes and time.

However, under the stricter test of constant mode amplitudes, while the model still provides accurate predictions for the remnant parameters and excellent residuals at the peak, some of the modes cannot be consistently extracted at times very close to the peak. An unmodeled, unidentifiable contribution to the waveform in the immediate postpeak region seems to spoil the stability of the modes when attempting to extract them numerically. The time at which we can show constant mode amplitudes appears to depend on the remnant spin, as the higher spin system requires a longer wait time. As can be seen in Sec. V, stable amplitudes are not achievable until $\sim 4M$ after the peak in a moderately spinning case and $\sim 8M$ postpeak in a high-spin case.[2]

There are multiple factors that may contribute to our inability to show constant mode amplitudes at early times in the ringdown. These include the prompt response [26,27], evolving QNM amplitudes [28,29], and effects not describable as perturbations of a single remnant black

---

[1]In this paper, the peak always refers to the peak amplitude of the (2, 2) mode of the strain. The time of this peak can differ significantly from that of other mode amplitudes, or of energy fluxes, or of quantities like Ψ_4.

[2]We note that these times correspond roughly to the times of the peak luminosity, over all (ℓ, m), for each system.

hole. In addition, recent works [30,31] showed that changes in the mass and spin of a perturbed black hole generate a nonlinear response in the QNMs early in the ringdown. Interestingly, Refs. [30,31] showed that despite this non-linear response, the resulting waveform is still well-modeled by a linear superposition of QNMs, which settle into constant amplitudes very early on. While Refs. [30,31] considered a perturbed single black hole, it is plausible that this effect also exists in binary mergers and that it might contribute to some of the unmodeled content in the early ringdown. Nevertheless, one of the main conclusions of this paper is that empirically all of these possible effects make small contributions to the strain observed at infinity.

It is worth emphasizing that the times referenced above refer specifically to the time at which we can show all mode amplitudes to be relatively stable. While the stability of many modes is influenced by the unmodeled content at earlier times, the $n \leq 2$ overtone amplitudes measured at the peak agree with the amplitudes recovered at the abovementioned times for each system. This suggests that these modes may still be identifiable in an analysis carried out at the peak. In Ref. [2], a Bayesian analysis exploring overtones in a LIGO-like detector showed that for realistic signal-to-noise ratios, a model with just the first few overtones at the peak is sufficient to accurately recover the remnant mass and spin. This is because the first few overtones can be resolved at higher levels of noise than the higher overtones. Determining the optimal time and the set of modes necessary for properly analyzing ringdown data for different systems and noise levels is left to future work. We discuss the issue of start time and the effect of early unmodeled contributions on the accuracy of our QNM model more in Sec. V D.

III. QUASINORMAL MODES

Linear perturbations of the Kerr metric describing a rotating black hole can be readily determined by solving a wave-type equation for a complex scalar Ψ by separation of variables [1,32]. The solution from doing so can be decomposed into multipoles $\Psi_{\ell m}$ by using spin-weighted spheroidal harmonics [1,32,33]

$$\Psi_{\ell m} \sim \int d\omega e^{-i\omega t} \sum_{\ell m} R_{\ell m}(r, \omega). \qquad (1)$$

Here the modes $R_{\ell m}$ are a solution of a radial equation analogous to a quantum mechanical radial equation with some effective potential. At large r, Ψ encodes the two independent polarizations of the gravitational wave h. The ringdown solution we seek for $R_{\ell m}$ describes radiation leaving the domain both at infinity and at the surface of the black hole—an eigenvalue problem for frequency ω. Since energy is being dissipated, the eigenfrequencies $\omega_{\ell mn}$ are complex. The index n labels the radial eigenvalues, with $n = 0$ corresponding to the least-damped mode, $n = 1$ the

next least damped, and so on. Modes for $n > 0$ are called overtones, although they have very different behavior than overtones in other physical systems. At late times, the $1/r$ piece of Eq. (1) at large r becomes an outgoing wave

$$\Psi_{\ell m} = \sum_{\ell mn} C_{\ell mn} e^{-i\omega_{\ell mn}(t - r_*)}, \qquad (2)$$

where r_* is a radial "tortoise" coordinate.

The gravitational wave strain h measured by a detector consists of two polarization states. These are usually combined into a single complex strain that is decomposed into modes using spin-weighted spherical harmonics. We will initially ignore the distinction between spherical and spheroidal harmonics, so the strain modes at a fixed large r_* are

$$h_{\ell m} = \sum_{n=0}^{\infty} C_{\ell mn} e^{-i\omega_{\ell mn}t}. \qquad (3)$$

In Eq. (3) we have renormalized the amplitudes $C_{\ell mn}$ in going from Ψ to h. Each term in this sum represents a damped sinusoid and gives the mathematical description of a single QNM with indices (ℓ, m, n). Note that $C_{\ell mn}$ refers specifically to the complex-valued amplitudes associated with each mode and that we use $A_{\ell mn} \equiv |C_{\ell mn}|$ to denote the absolute value of the mode amplitudes.

A. QNM notation

The Schwarzschild metric is symmetric under the transformation $t \to -t$. Accordingly, the QNMs for a given (ℓ, m) come in pairs with positive and negative oscillation frequencies: $\omega_{\ell mn} = -\omega_{\ell mn}^*$. The negative-frequency mode is called a mirror mode, since it is a reflection across the imaginary frequency axis of the positive-frequency mode. For the Kerr metric, the symmetry transformation is $t \to -t, \phi \to -\phi$. The QNMs still come in pairs, but the symmetry relation is now $\omega_{\ell mn} = -\omega_{\ell -mn}^*$. Thus it is the positive-frequency mode for $-m$ that generates the negative-frequency partner for the original mode. Note that because of these relations, tables of QNM frequencies typically only give the positive-frequency values.

QNMs can also be described as prograde or retrograde. A prograde mode has m and the real part of ω with the same sign, so with the dependence $\exp(-i\omega t + im\phi)$ the pattern speed is in the direction of increasing ϕ.

The amplitudes of the QNMs depend on how the modes are excited. For typical binary black hole mergers, such as those considered in this paper, the angular momentum in the system ensures that the prograde modes are excited more strongly than the corresponding retrograde modes.

In this paper, we will use the notation (l, m, n) to denote a QNM, adhering to the convention that its real part is always positive. For example, (2, 2, 0) corresponds to the prograde fundamental mode $e^{-i\omega_{220}t}$, while $-(2, -2, 0)^*$

represents a retrograde mode $e^{i\omega_{2,-2,0}^* t}$. The values of ω_{220} and $\omega_{2,-2,0}$ are taken from the typical tables of QNM frequencies. Appendix A gives additional details about QNM notation.

B. Fitting damped sinusoids

A key feature of the work reported here is that we do *not* use standard nonlinear least-squares algorithms to fit QNMs to our numerical waveforms. Fitting a sum of damped sinusoids to data is a tricky problem. Note that a single damped exponential can be written in several equivalent forms:

$$Ae^{-i(\omega t+\phi)} = Ae^{-i\phi}e^{-i\omega t} = Ze^{-i\omega t}, \qquad (4)$$

$$Z = Ae^{-i\phi} \equiv x + iy. \qquad (5)$$

Here A and ϕ are real, while ω can be complex. If ω is known, then using the first expression in Eq. (4) requires nonlinear least squares to fit for the phase ϕ, whereas the last expression in that equation makes clear that the problem actually requires only linear least squares fitting. However, fitting for the frequencies, whether real or complex, is inherently a nonlinear least squares problem and generally much more difficult.

The next important point is that fitting a sum of exponentials with unknown frequencies or decay constants is numerically ill-conditioned. This fact has been known for a long time (see, e.g., the 1956 book by Lanczos [34]), and is continually rediscovered by physicists. In practice, this means that fitting with the wrong number of exponentials or with the correct number but noisy data, can lead to results with large errors. This sensitivity implies that one needs to use as robust a method as possible to do the fitting.

The "best" algorithm known has also been known for a long time, since 1973 [35]. It takes advantage of the fact that some of the parameters in the fit enter the model linearly while others are nonlinear. Such problems are called separable least squares, and the algorithm is called Variable Projection, implemented originally in a Fortran code called VARPRO [36]. The idea is to start with initial guesses only for the nonlinear parameters. Then standard linear least squares solves for the linear parameters by the usual analytic process. Next, an iterative nonlinear fitting routine updates the nonlinear parameters with the linear parameters held fixed. The whole procedure is then iterated until a suitable tolerance is achieved. The clever part of the algorithm deals with the Jacobian of the cost function with respect to the nonlinear parameters that is used in the nonlinear fitting. This Jacobian has a dependence on the linear parameters because the nonlinear parameters depend implicitly on the linear ones. Reference [35] worked out this contribution to the Jacobian—it can be computed explicitly from the analytic solution of the linear least-

squares problem using linear algebra techniques. In general, this algorithm is never worse than brute-force nonlinear least squares fitting, and often succeeds when brute force fails.

Although most of the main results we present in Sec. V are obtained from simple linear least-squares fits, VARPRO is crucial in arriving at these results. The ringdowns we analyze are composed of an initially unknown number of overlapping individual quasinormal modes with unknown frequencies and damping times. While VARPRO is the best algorithm we know of to tackle this problem, it is still challenging to simultaneously identify many modes in the presence of numerical noise when the number of modes and their frequencies are unknown. To simplify the problem, we rely on the fact that many modes decay at different rates and that the majority of the modes will have decayed below the noise floor at late times. Given this, we initially employ VARPRO at very late times where only one or two long-lived modes are still present and allow VARPRO to identify modes agnostically, determining the complex frequencies and complex amplitudes of the slowest decaying modes.[3] Once we are confident in the presence and stability of these modes, we move to a slightly earlier time and look for the next slowest decaying modes. To further simplify the fitting, as we step back to an earlier time and agnostically search for additional modes, we no longer allow the frequencies of previously found modes to vary. Instead, we keep them fixed at the analytic values corresponding to the remnant mass and spin. This reduces the complexity of the fit to one or two nonlinear searches at a time, while previously found modes enter into the fit linearly. We repeat this process of adding found modes and nonlinearly searching for new modes until VARPRO can no longer find any stable modes.

Finally, in regards to initial guesses, when the number of modes is reasonable and VARPRO is well-behaved, it is insensitive to the initial guess when searching for new modes. Given this, we set the initial guess for the real part randomly from the interval $[0, 1)$ and the imaginary part from an interval of $(-1, 0]$, which are practical values for the ringdown frequencies of the waveforms considered in this work. While VARPRO is capable of imposing bounds, we set the bounds for the real and imaginary components to be $(-\infty, \infty)$, effectively allowing the search to be unbounded.

In this work, we have relied on a modern implementation of VARPRO [37] in Matlab. We have translated this code into Python so that it can use the nonlinear solvers available in Scipy. This Python version is publicly available at [38].

---

[3]Note that we use varying time intervals to identify stable new modes that show up as we go back in time. These intervals are longer at later times and shorter at earlier times, when multiple new modes with rapid decay times appear.

IV. METHODS

A. Waveform data

For our comprehensive ringdown analyses, we use two binary black hole simulations [39], whose inspiral and remnant parameters can be found in Table I. The Cauchy evolution of these simulations is performed using the SpEC code [40], while the waveform and the Weyl scalars are computed at future null infinity by running the SpECTRE code's Cauchy-characteristic evolution (CCE) code [14–16]. We then map the waveform data at future null infinity to the superrest frame of the remnant black hole $250M$ past the luminosity peak using the package SCRI [17,19,20,41–43]. We stress that this component of the postprocessing that fixes the BMS frame is absolutely crucial for performing robust and accurate ringdown analyses. By mapping the asymptotic data to the superrest frame of the remnant black hole, one ensures that the remnant is at the origin, at rest, has its spin aligned with the $\hat{z}$-axis, and is not supertranslated relative to the usual Kerr metric. Thus, there can be no unexpected mode mixing between the spherical harmonic modes, which would complicate the QNM fits, as was found in, e.g., Refs. [7,13].

Once the strain and the Weyl scalars are obtained at future null infinity in the superrest frame of the remnant black hole, we utilize SCRI to perform one more postprocessing step that simplifies the ringdown analyses. As outlined in Eq. (12) of Ref. [44] as well as elsewhere in Refs. [45–47], because of the supertranslation symmetry at future null infinity, the strain obeys the supermomentum balance law

$$h = \frac{1}{2}\bar{\eth}^2\mathfrak{D}^{-1}\left[-\left(\Psi_2 + \frac{1}{4}h\,\bar{h}\right) + \frac{1}{4}\int_{-\infty}^{u}|\dot{h}|^2 du\right]. \quad (6)$$

The notation here is that of Ref. [44] and is not important for this paper, other than to note that h is the strain. The first term in Eq. (6) is related to the Bondi mass aspect and is effectively a combination of the mass and the current multipole moments. The second term in Eq. (6) corresponds to an energy flux and is often interpreted as the source of the null memory [44,48–56]. It is a purely nonlinear contribution in the sense that it depends on the strain quadratically. Consequently, when fitting the strain

TABLE I. Inspiral and remnant parameters for the two binary black hole simulations used in our ringdown analyses. Here q is the mass ratio and χ_z is the z-component of the BH spin. In both simulations, the binaries are of equal mass and the BH spins are aligned with the orbital angular momentum. The remnant parameters are the final mass M_f and the final BH spin χ_f.

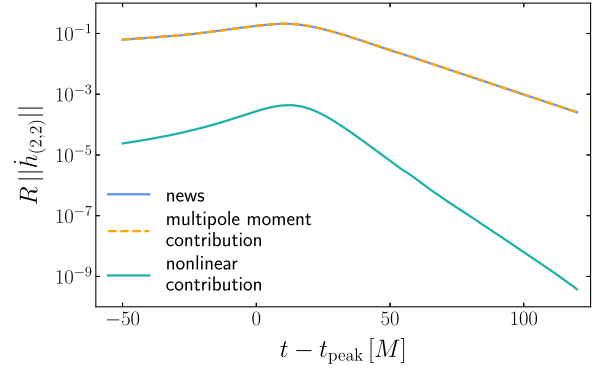| SXS ID	q	χ_{1z}	χ_{2z}	M_f	χ_f
BBH:2420	1.0	0.2	0.2	0.95	0.75
BBH:2423	1.0	0.85	0.85	0.91	0.92

FIG. 1. The (2, 2) component of the news and the two terms of Eq. (6) that contribute to the news for SXS:BBH:2423. The news and the contribution from the multipole moment, the first term in Eq. (6), overlap and are effectively indistinguishable. The nonlinear contribution, which is a few orders of magnitude smaller than the news, is also shown. This nonlinear contribution refers to the energy flux described in Sec. IV A and corresponds to the second term in Eq. (6).

with linear QNMs, this term raises the effective noise floor, as it can only be modeled with second-order QNMs.[4] Because of this, rather than fitting the full strain, which includes this nonlinear contribution, we instead only fit the contribution to the strain coming from the first term in Eq. (6). Although this term will still have nonlinear QNM contributions that we will have to fit, by neglecting the contribution from the null memory the fits should be more straightforward to carry out. Finally, because of residual supertranslations that may exist from the BMS frame fixing being imperfect, instead of fitting the strain (which can be shifted by a constant), we fit the news, i.e., the first time derivative of the strain.

To help clarify this point regarding the nonlinear term, in Fig. 1 we show the (2, 2) mode of the news as well as the contributions from the multipole moments and the nonlinear term in Eq. (6). As is clearly illustrated, the nonlinear term in Eq. (6) is three orders of magnitude smaller than the full news. Consequently, since this term would simply detract from our ability to resolve overtones by including certain extra, nonlinear contributions, we do not include it in the waveforms that we fit in this work.

Finally, the last step in preparing the waveforms to be fit with QNMs is to adjust the scale of the time coordinate (and hence the derived frequencies) to match the convention in tabulated values. This step is unfortunately often ignored in the literature, but is key for performing robust and accurate black hole spectroscopy. In particular, SpEC uses the total Christodoulou mass of the binary as the mass unit, whereas tables set the mass unit to unity. Thus the time coordinate of

---

[4]In particular, this term measures the null memory sourced by QNMs and should be dominated by the second-order QNM $(2, 2, 0) - (2, 2, 0)^*$ for typical binary black hole mergers.

SpEC waveforms must be multiplied by the total Christodoulou mass. Even though this mass is typically within 10^{-4} of unity, failing to make this correction can strongly bias QNM fits.

B. Fitting

Identifying the modes present in the ringdown of an arbitrary numerical waveform comes with a number of challenges. To illustrate these challenges, we first consider an idealized analytic ringdown model. We construct an analytic waveform modeled after the ringdown of SXS: BBH:2423 and its remnant parameters. The analytic model is a superposition of modes, as in Eq. (3), including the $(2,2,n)$ modes with $n = \{0\dots9\}$, the $(3,2,0)$ mode and its first overtone, the $(3,2,1)$ mode. In addition to these damped sinusoids, we also add a constant term to help stabilize our fits, since such a term seems to be present in our numerical relativity waveforms for reasons that are not clear. The constant we fit tends to be three orders of magnitude smaller than the smallest damped sinusoid, which emphasizes the ill-conditioned nature of the fitting. The frequencies, $\omega_{\ell mn}$, are determined by the remnant of SXS:BBH:2423 and the complex amplitudes, $C_{\ell mn}$, are consistent with those we find below in SXS:BBH:2423.

In such a purely analytic model, we can use linear least squares with varying start times to fit for the modes we have included. We recover the expected amplitudes as they decay over time until they eventually reach roundoff. However, in realistic numerical waveforms, numerical noise interferes with the ability to resolve the individual modes below some level. In order to better understand the role of numerical noise, we add a small amount of Gaussian noise to the analytic model. In this particular example, we add Gaussian noise with an average amplitude of $\sim 2 \times 10^{-8}$. For context, the numerical noise often present in SXS extrapolated waveforms is closer to 10^{-4}–10^{-5}, so the amount of noise added in this example is orders of magnitude smaller than that present in publicly available waveforms.

The results of this procedure are shown in Fig. 2. Notice that while the least damped modes are well resolved across a wide range of times, the highest damped modes are most sensitive to the tiny amount of noise we have added. In Fig. 2, the $n = 9$ and $n = 8$ modes are the first to be affected by the added noise, deviating from their expected decays at around 12–13M. Although the noise is only around 10^{-8}, these modes become unresolvable at much larger amplitudes, $\sim 10^{-3}$ for $n = 9$ and $\sim 10^{-2}$ for $n = 8$. Once the higher damped modes begin to deviate, the next highest damped modes are eventually affected and the deviations cascade through the lower n, yielding inaccurate amplitudes for many of the modes. This high sensitivity to low noise levels even in analytic models means that highly damped modes are likely to be very difficult to resolve in even the best numerical waveforms publicly available, *and even when they are really present.*

The early deviation from the expected decay that occurs for some of the mid-range n, say $n = 5$, is in part due to the higher modes, $n > 5$, becoming unresolvable yet remaining in the set of modes we use to fit to the data. For example,
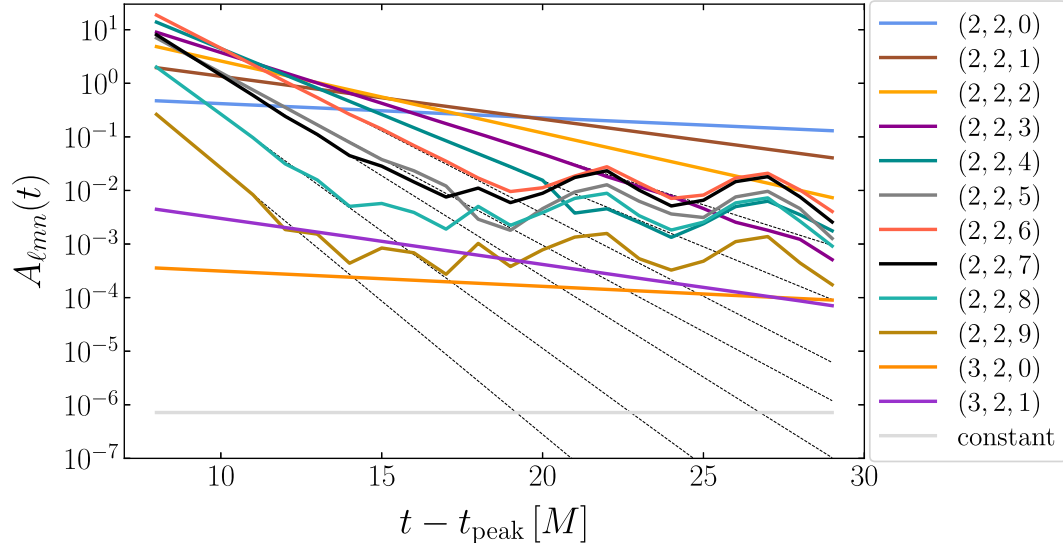

FIG. 2. Mode amplitudes as a function of time, recovered from a linear least-squares fit to an analytic waveform in the presence of Gaussian noise at a level of $\sim 10^{-8}$. The modes included are various $(2,2,n)$ and $(3,2,n)$ modes with amplitudes and phases modeled from SXS:BBH:2423, as well as a constant term with an amplitude of $\sim 5 \times 10^{-7}$. The recovered amplitudes are the solid colored lines, while the black dotted lines represent the analytic expectations for each mode. Notice that once the $(2,2,9)$ mode begins to deviate from its analytic value because of the small amount of added noise, other highly damped modes eventually follow suit. This extreme sensitivity to low-level noise is one of the primary challenges to stably resolving highly damped QNMs.
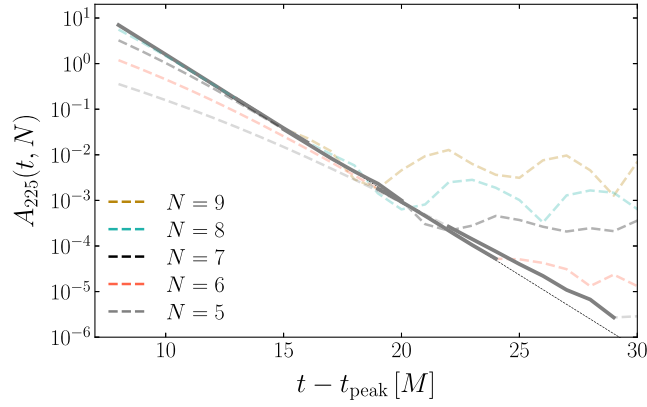
FIG. 3. The (2, 2, 5) mode amplitude recovered from a linear least-squares fit to the same analytic waveform shown in Fig. 2. The solid gray line is a composite amplitude of the $n = 5$ mode obtained through the process of dropping higher modes once they become unstable due to noise. Each dashed curve shows the $n = 5$ amplitude recovered from a fit including up to N overtones of the $(2, 2, n)$ QNMs. Notice that the curve associated with $N = 9$ is the first to deviate from the expected decay and that models with a lower N at later times are in better agreement with the analytic expectation. This dropping of modes results in improved mode amplitude extraction, extending the amplitude down a few orders of magnitude and out an additional $\sim 10M$ compared to just fitting with $N = 9$.

consider Fig. 2, where we are fitting up to $N = 9$, where N denotes the maximum overtone number n used in a fit. We see how the $n = 5$ mode begins to deviate from its expected decay at around $16M$, when its amplitude is still 10^{-2}. This is well above the amplitude for which we are able to resolve the highest damped mode, $n = 9$. One remedy for this issue is to discard the highest modes once they are affected by the noise, which in turns extends our ability to resolve some of the lower modes. In practice, this means that once we reach a time where the $n = 9$ mode can no longer be resolved for a given noise level, the set of $(2, 2)$ modes that we include in the fit is limited to $N = 8$ rather than $N = 9$. Similarly, once we reach a time where the $n = 8$ mode has reached its limit, we drop that mode and limit the set to $N = 7$.

In Fig. 3, we show how this process of dropping higher modes leads to better resolvability of lower modes, and in this particular case, the $n = 5$ mode. There are five different curves in Fig. 3, each corresponding to the amplitude of the $n = 5$ mode when the fit is limited to just N overtones of the $(2, 2)$ mode. The $N = 9$ curve is identical to the $n = 5$ curve of Fig. 2, as that fit includes up to $N = 9$ overtones. Notice in Fig. 3 that each time N is reduced, the $n = 5$ mode can be resolved at a lower amplitude than the previous N. To distinguish the regions where certain N are valid, each dashed curve is overdrawn with a solid gray curve when it is the preferred set. Once the fitting process with mode dropping is complete, we are left with a composite $n = 5$ amplitude that now extends down to roughly 10^{-5} and out to about $29M$. So, through the

process of dropping modes, we extend our ability to resolve this particular mode by three orders of magnitude in the amplitude and increase the time over which it is resolved by $\sim 10M$. A direct comparison can be made by comparing the gray composite amplitude with the dashed $N = 9$ curve, which corresponds to the best resolvability of $n = 5$ in the absence of mode dropping.

Although we focused here on the $n = 5$ mode of the analytic example, the process of dropping modes leads to better resolvability of all modes. This is because including modes in the fit that are no longer present in the data spoils the resolvability of those modes still present. We find through this analytic example that the process of dropping modes is critical to properly resolving modes. This example also emphasizes the ill-conditioned nature of fitting damped sinusoids to data. In the next section, we use this same technique to properly resolve the modes of numerical relativity waveforms.

V. RESULTS

Having described our methods for identifying modes with VARPRO in Sec. III B and our mode-dropping technique in the previous section, we now turn to identifying and fitting the QNMs of two high-accuracy numerical relativity waveforms. In particular, we study one highly spinning remnant, SXS:BBH:2423, and one more moderately spinning remnant, SXS:BBH:2420. The binary and remnant parameters for each simulation are listed in Table I. For each waveform, we use VARPRO to identify the QNMs present in the ringdowns. We do this by starting at late times and working our way backward, letting VARPRO identify the best-fitting frequency and damping times at each point in time. Each time we find a stable frequency and damping time that corresponds to a QNM associated with the asymptotic remnant parameters, that QNM is permanently added to the fitting set. Previously found modes then enter into the fit linearly alongside a nonlinear search for additional modes through VARPRO. We continue this process until no additional stable modes are found. With this procedure, we are able to identify a large set of stable QNMs in both simulations. These modes include a large number of overtones, multiple modes from spherical-spheroidal mixing, and a number of second-order QNMs.

Note that there are two distinct fitting procedures used to obtain the following results. The first procedure involves nonlinear fitting using VARPRO to identify the QNMs in a particular waveform, as described above. The second fitting procedure is a linear least squares method coupled with a mode-dropping technique to show the stability of the QNMs identified through VARPRO in the first step. This second procedure is critical to show the stability of QNM amplitudes in the presence of numerical noise as highlighted in the simplified analytic case within Sec. IV B.
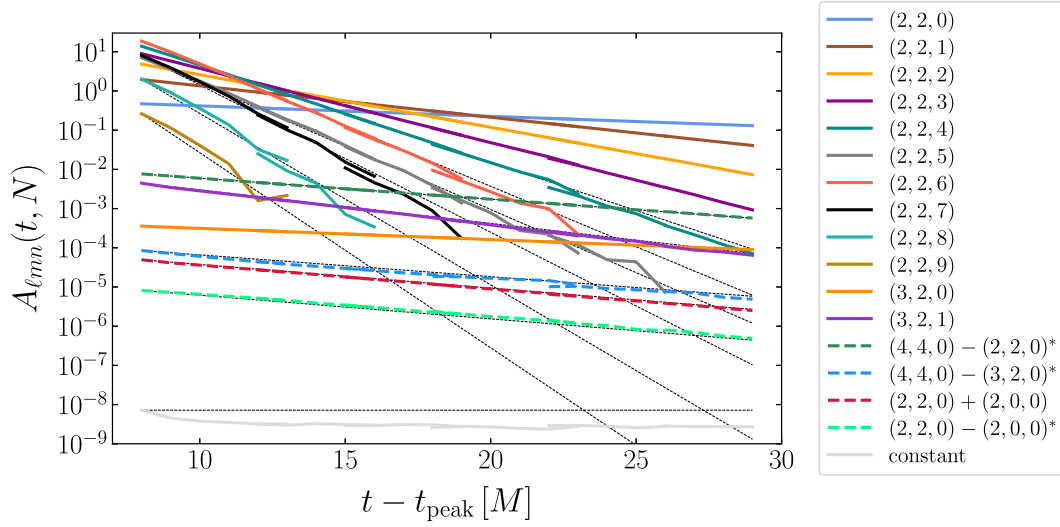
FIG. 4. QNM amplitudes as a function of time from linear least-squares fits of the (2, 2) component of SXS:BBH:2423. The linear QNMs are denoted by solid lines while the second-order QNMs are indicated by dashed lines. Here again, the dotted black lines represent the expected analytic decay of each mode. The discontinuities in the amplitudes are due to the mode-dropping technique that was shown to improve mode extraction in the analytic model considered in Sec. IV B. At each point where a QNM's amplitude ends discontinuously, this means that mode has been dropped from the set of modes in the fit. This is the case for the highest-damped modes, which are more easily affected by the numerical noise present in the NR waveforms. Aside from these modes, which eventually get dropped, the remaining QNMs are well resolved over a significant window of time. The majority of the second-order QNMs are subdominant to all linear contributions, except for the $\omega_{440} - \omega_{220}^*$ QNM. This particular QNM, with its larger amplitude and relatively slow decay, is a good candidate for probing nonlinear contributions to ringdowns in future gravitational wave observations.

A. High-spin NR ringdown

The first case we consider is SXS:BBH:2423, in which the QNMs decay more slowly because of its more rapidly spinning remnant. This property of high-spin remnants means that the more rapidly decaying overtones are longer lived and therefore more easily resolvable. We show a numerical decomposition of the ringdown of SXS: BBH:2423 into its individual modes in Fig. 4. We see that the ringdown contains a multitude of QNMs, including the fundamental (2, 2, 0) mode and nine of its overtones, the (3, 2, 0) mode and one of its overtones, and four second-order QNMs. For each mode, we include a dotted line indicating the expected analytic decay, which is the path a stable well-resolved mode should follow. The discontinuities in the amplitudes of the individual modes are a consequence of the mode dropping technique we employ, which is necessary because of the numerical noise present and was discussed in more detail in Sec. IV B.

A surprising aspect of this result is the presence of four previously unidentified second-order QNMs, which are all exceptionally stable. A second-order QNM, or quadratic QNM, is generated from the product of two linear QNMs. So its frequency is a sum or difference:

$$\omega = \omega_{\ell_1 m_1 n_1} + \omega_{\ell_2 m_2 n_2} \quad \text{or} \quad \omega = \omega_{\ell_1 m_1 n_1} - \omega_{\ell_2 m_2 n_2}^*.$$

These would lead to modes with $m = m_1 + m_2$ and $m = m_1 - m_2$. The modes we find that satisfy $m = 2$ in

this ringdown are $\omega_{440} - \omega_{220}^*$, $\omega_{440} - \omega_{320}^*$, $\omega_{220} + \omega_{200}$, and $\omega_{220} - \omega_{200}^*$. All of these modes are denoted by dashed lines in Fig. 4. While the real part of the second-order QNM frequency is the sum or difference of the real parts of the linear QNMs, in both of the above cases, the imaginary part of the second-order QNM is always the sum of the imaginary components of the linear QNMs. Thus, second-order QNMs decay more quickly than the linear QNMs they are generated from. Consequently, as can be seen in Fig. 4, the second-order QNMs decay more quickly than the fundamental mode, but more slowly than the overtones. This property of quadratic QNMs means that they occupy regions of the complex plane that make them reasonably easy to identify when relying on VARPRO to find modes. Moreover, while the second-order QNMs are subdominant to the overtones at early times, some of these modes remain measurable in the ringdown after most of the overtones have decayed away. This means that even at fairly late times in the ringdown, for a system like SXS: BBH:2423, the fundamental remains accompanied by the (2, 2, 1), the (3, 2, 0), and the $\omega_{440} - \omega_{220}^*$ second-order QNM. This means that, even at late times, a multimodal analyses of the ringdown may well be required with future high-accuracy detectors.

It is important to note that the data in Fig. 4 begins at $t = t_{\text{peak}} + 8M$. This is because, before this time, VARPRO can no longer reliably identify any additional stable complex frequencies. There appears to be some additional
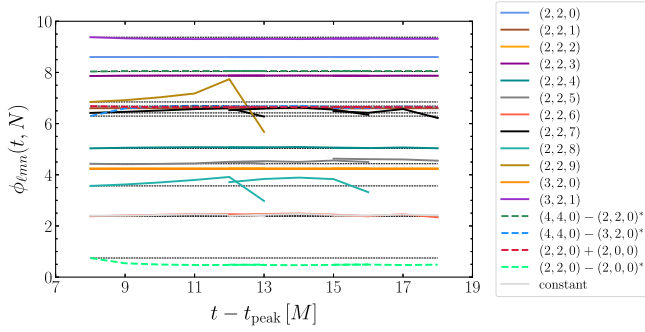
FIG. 5. QNM phases as a function of time from linear least-squares fits of the (2, 2) component of SXS:BBH:2423. The phases are obtained from the fits shown in Fig. 4 and the line styles here are consistent with that caption. The discontinuities in the phases of the higher damped QNMs are caused by the mode dropping described in the caption of Fig. 4. The phases are generally constant, with the higher overtones deviating first because of their sensitivity to numerical noise. We have not mapped the phases back to a conventional 2π range to improve distinguishability.
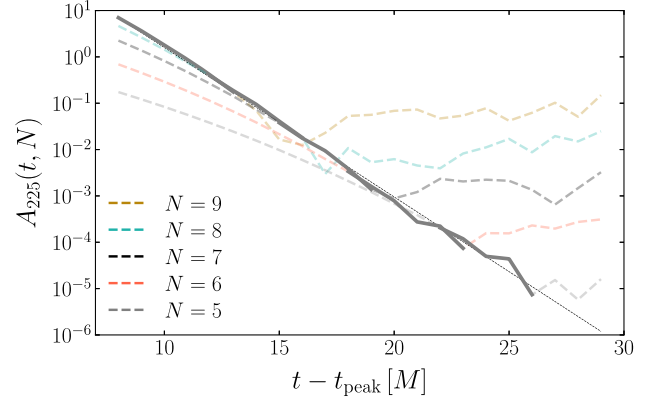

FIG. 6. The (2, 2, 5) mode amplitude recovered from linear least-squares fits to the (2, 2) mode of SXS:BBH:2423. The solid gray line is a composite amplitude of the $n = 5$ mode obtained through the mode dropping process. Each dashed curve shows the $n = 5$ amplitude recovered from a fit including up to N overtones of the $(2, 2, n)$ QNMs. This result is consistent with the example of extracting higher n from an analytic ringdown shown in Fig. 3 and described in Sec. IV B. The recovered amplitude is in good agreement with the expected analytic decay (black dotted line), spanning roughly five orders of magnitude in the amplitude over a range of $15M$.

content in this region of the ringdown, but it is apparently not well-modeled by a damped sinusoid with a fixed frequency. Consequently, performing a decomposition before this time results in unstable mode amplitudes, especially for the highest-damped modes, which are extremely sensitive to small amounts of noise or unmodeled data. One possible issue related to stably decomposing modes earlier than $8M$ is that some of the (ℓ, m)'s contributing to second-order QNMs do not peak until after the peak of the (2, 2). For instance, the $\omega_{440} - \omega_{220}^*$ QNM is sourced by the (4, 4, 0) mode, yet the (4, 4) contribution to the strain does not peak until $\sim 7.5M$ after t_{peak}. In fact, the average peak flux over the two-sphere occurs $\sim 10.5M$ after the peak of the (2, 2), which indicates some second-order contributions are likely still being sourced and are not well modeled by a constant exponential decay.

Finally, one additional check on the stability of modes is to check the phases of each QNM, as these should remain constant over time. In Fig. 5, we show the phase of each mode over a window of $10M$, where it is apparent that the most stable modes have constant phases throughout. As was the case with the amplitudes, the most quickly decaying overtones are the first to become unstable, which can be seen in the deviation of the phases from their initial values.

B. High-spin $n = 5$ QNM

In Fig. 6 we show the stability of the $n = 5$ mode in the ringdown of SXS:BBH:2423, a particularly challenging mode, which we can resolve over nearly $20M$ and across more than five orders of magnitude in the amplitude, showing consistency with the expected decay for a remnant with $\chi = 0.92$. We highlight this mode because of its high

overtone number and its anomalous behavior in the set of (2, 2) QNMs. This particular mode exhibits peculiar behavior with respect to the other n in its frequency and excitation factors for very high spins. In Appendix B, we discuss this mode further and explore the relationship between mode amplitudes and excitation factors.

C. Moderate-spin NR ringdown

Next, we consider SXS:BBH:2420, a system with a more moderately spinning remnant, specifically $\chi = 0.75$. This remnant spin is more representative of typical binary mergers and is closer to the remnant spin of a GW150914-like merger. Since the spin is lower, the QNMs decay more quickly than those of the system we considered in Sec. V A.

Employing the same methods used in Sec. V A, including the mode dropping method of Sec. IV B, we present a numerical decomposition of the QNMs in the ringdown of SXS:BBH:2420 in Fig. 7. What immediately stands out here in comparison to Fig. 4 is a significant increase in the number of modes present. As these simulations have different binary configurations, the initial conditions at the onset of the ringdown result in a different excitation of modes.

As Fig. 7 shows, we find many of the same modes present in SXS:BBH:2423, namely the (2, 2, 0) mode and many overtones, the (3, 2, 0) QNM and its first overtone, and the same second-order QNMs. However, we also find additional modes that do not appear in the ringdown of SXS:BBH:2423. These include a second overtone
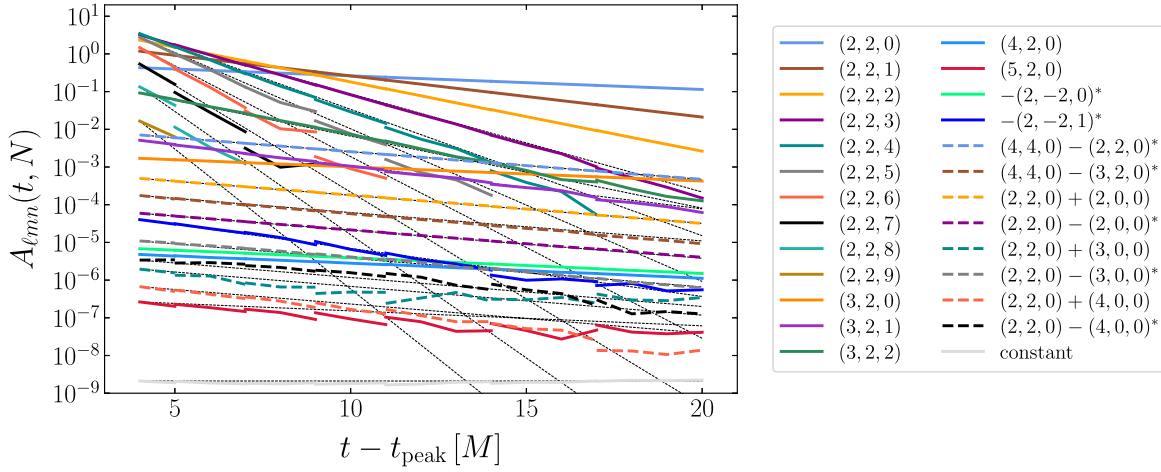
FIG. 7. QNM amplitudes as a function of time from linear least-squares fits of the (2, 2) component of SXS:BBH:2420. The linear QNMs are denoted by solid lines while the second-order QNMs are indicated by dashed lines. The dotted black lines again represent the expected analytic decay of each mode. As detailed in the caption of Fig. 4, the high-spin case, the discontinuities in the amplitudes are caused by dropping certain fast-decaying QNMs. The amplitudes of the highest overtones are more difficult to resolve in this lower-spin case because of the increased number of modes and the increased damping that comes with lower spins. Additionally, the lowest-amplitude modes are also more challenging to resolve, especially as they decay further into the numerical noise. Aside from this, the majority of the first- and second-order QNMs are well resolved. Note that there are a number of additional modes present in this simulation as compared to the higher-spin case, including some retrograde modes, higher overtones of the (3, 2), and four additional second-order QNMs. Here again, the $\omega_{440} - \omega_{220}^*$ QNM is the dominant second-order mode, indicating that this mode in particular may be an ideal candidate for future gravitational wave observations.

associated with the (3, 2, 0) mode, the (3, 2, 2), and some additional QNMs from spherical-spheroidal mixing, the (4, 2, 0) and (5, 2, 0). Interestingly, we also find four additional second-order QNMs, in particular: $\omega_{220} + \omega_{300}$, $\omega_{220} - \omega_{300}^*$, $\omega_{220} + \omega_{400}$, and $\omega_{220} - \omega_{400}^*$. The final two additional modes present here are the retrograde QNM $- \omega_{2,-2,0}^*$ and its first overtone $-\omega_{2,-2,1}^*$.

As was the case for SXS:BBH:2420, many of the (2, 2) overtones are well resolved, aside from the quickest decaying modes such as the $n \geq 7$ QNMs, which are highly susceptible to small amounts of noise. These QNMs are also more sensitive to the dropping of the next highest mode, leading to larger discrepancies in the amplitudes measured before and after the drop. The (3, 2, n) modes are all very well resolved, including the (3, 2, 2), which is the first time this mode has been found in the (2, 2) harmonic. While the (4, 2, 0) QNM is easily measurable, the (5, 2, 0) mode has a very small amplitude, making it challenging to cleanly extract. The two retrograde modes, which are apparently swallowed up in the higher-spin case, are both relatively stable. A Fourier transform of the ringdown signal confirms that these modes reside on the opposite side of the frequency axis relative to the (2, 2, n) QNMs.

As for the second-order QNMs, the highest amplitude modes are as stable as many of the first order QNMs, but the lower amplitude modes are somewhat susceptible to noise. Notice in Fig. 7, that the $\omega_{440} - \omega_{220}^*$ QNM is again the highest amplitude quadratic mode and of sufficient amplitude that it will survive until late in the ringdown,

subdominant only to the (2, 2, 0), (2, 2, 1), and (3, 2, 0). The three other second-order QNMs, $\omega_{440} - \omega_{320}^*$, $\omega_{220} + \omega_{200}$, and $\omega_{220} - \omega_{200}^*$ that were also present in SXS:BBH:2423, have moderate amplitudes that remain stable throughout. Notice though that while the $\omega_{440} - \omega_{320}^*$ QNM was larger than the $\omega_{220} + \omega_{200}$ QNM in the higher spin case, the order of these two modes is flipped in this ringdown. The remaining four second-order QNMs, ordered by amplitude are $\omega_{220} - \omega_{300}^*$, $\omega_{220} - \omega_{400}^*$. $\omega_{220} + \omega_{300}$, and $\omega_{220} + \omega_{400}$. While the first two are relatively stable throughout, the two at lower amplitude become noisy as they decay further into the noise.

The data in Fig. 7 does not start at t_{peak}, but instead at $t = t_{\text{peak}} + 4M$. As was the case with SXS:BBH:2423, VARPRO cannot identify a stable frequency before this time. We suspect this is likely for the same reasons discussed in Sec. VA, namely unmodeled content and sourcing of the second-order modes. Here, the (4, 4) does not peak until $\sim 4.5M$ after t_{peak} and its average peak flux over the two-sphere is $\sim 7M$ after the (2, 2) peak. Once again, stable amplitudes are achievable roughly around the time the (4, 4) peaks. Although we suspect this contributes to the instability of amplitudes early on, additional nonlinearities may also play a role here. In the two cases, the time until stable amplitudes are achieved appears to follow the usual relationship between remnant spin and decay rates, meaning that any nonlinearities should decay away more slowly in the higher-spin case and more quickly in the lower-spin case, as we see here.

D. Remnant parameters

So far, we have used the NR asymptotic remnant mass and spin, M_f and χ_f, to determine the QNM frequencies, $\omega(M_f, \chi_f)$, used in our fits. To test whether this is indeed the best-fitting M and χ, we repeat the fits while allowing these parameters to vary and inform the QNM frequencies through $\omega(M, \chi)$. In the end, the best-fitting M and χ is the set that produces the smallest residual—keeping in mind that the underlying mass and spin as measured in the NR simulation are unknowns in this process. To see how the best-fitting M and χ compare to the NR quantities, M_f and χ_f, we use

$$\epsilon = \sqrt{(\delta M_f/M)^2 + (\delta \chi_f)^2} \qquad (7)$$

as our measure of error, where δM_f and $\delta \chi_f$ are the differences between the best-fit values and the NR measured quantities. This allows us to quantify how well the model predicts the true underlying asymptotic remnant quantities and to explore the performance of the model at different times in the ringdown.

We begin with a focus on the ringdown of the high-spinning remnant of SXS:BBH:2423. At each point in time, we fit a set of QNMs to the data and find the best combination of M and χ that minimizes the residual. We then compute the corresponding ϵ from Eq. (7). In Fig. 8, we show ϵ for a range of models over a range of $30M$ starting from t_{peak}. All of the modes used in the fits of Fig. 4
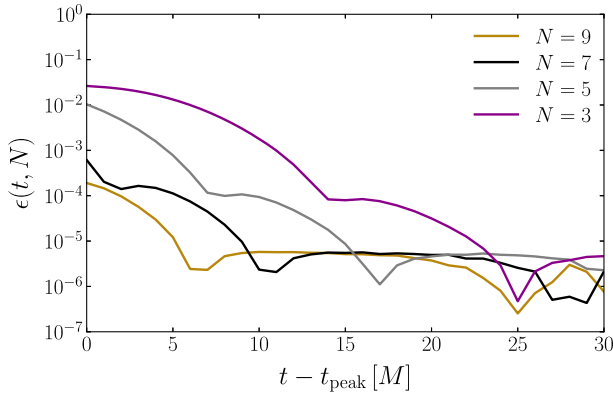
are again used here, but we limit the set of $(2, 2, n)$ modes to $n = \{0, \ldots, N\}$, where N is the maximum n included in the fit. In Fig. 8, we find that when the appropriate N is used, the model predicts the remnant quantities remarkably well, with $\epsilon < 10^{-5}$. This small deviation from the NR remnant quantities indicates how well the QNM model fits the data and reflects the predictive power of accurate fitting. Fig. 8 also allows us to explore the shortcomings of a given model by observing when ϵ deviates from the minimum achievable values. For instance, considering $N = 3$, we see that ϵ is as large as $\sim 10^{-2}$ at early times and does not achieve 10^{-5} until $\sim 25M$. This is because many overtones present in the data earlier on are not included in the set used for fitting and it is not until those modes have decayed away does $N = 3$ become the appropriate model. The results and reasoning are similar for the other N.

While the deviations in ϵ for $N = \{3, 5, 7\}$ in this example are understood to be caused by ignoring overtones present in the data, the case of $N = 9$ is less well understood. In Fig. 8, we see that for $N = 9$, ϵ stabilizes around 10^{-5} about 8–9M after the peak. This is consistent with our ability to show stable amplitudes after this time in Fig. 4. However, before this time, we see ϵ deviates from this minimum value and rises to 10^{-4} by t_{peak}. This again tells us that there is unmodeled content in this region that we are not currently including in the fit. This is consistent with the discussions in the two previous sections on unstable amplitudes at early times, where we speculate this is caused
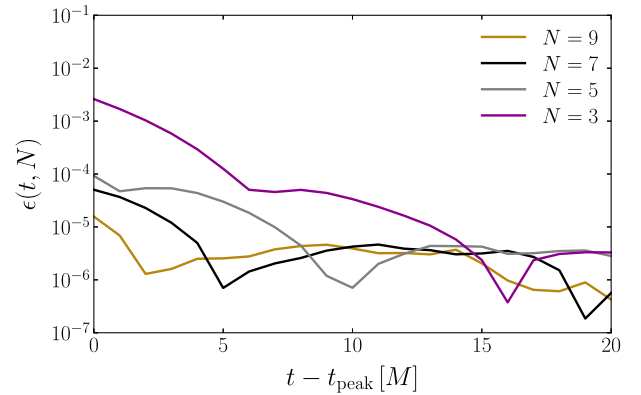

FIG. 8. Measure of error ϵ, defined in Eq. (7), as a function of time for different N. This measure of error quantifies the difference between the best-fit mass and spin versus the NR asymptotic remnant mass and spin for SXS:BBH:2423. Each fit includes the set of QNMs shown in Fig. 4, but with the $(2, 2, n)$ modes limited to a maximum N overtones. There is a floor near 10^{-5} that each N reaches once that model is preferred. The $N = 9$ set accurately predicts the remnant quantities at a level of 10^{-4} at t_{peak} and eventually reaches the 10^{-5} floor near the time at which we can show stable amplitudes in Fig. 4. The other N eventually reach similar values once the higher overtones excluded from those sets have sufficiently decayed away.

FIG. 9. Measure of error ϵ, as defined in Eq. (7), for SXS:BBH:2420. As detailed in the caption of Fig. 8, this quantity measures the error in the mass and spin preferred by each set of QNMs compared to the true NR asymptotic remnant mass and spin. Here, as in Fig. 8, each N reaches a floor below 10^{-5} once that model is optimal. In this case, each N produce smaller values of ϵ at t_{peak} compared to those in Fig. 8, which is consistent with finding stable amplitudes at an earlier time compared to the higher spin case. Similarly, each N reaches the 10^{-5} floor earlier, since the QNMs for this case are more highly damped. Although $N = 9$ does not reach a minimum until $\sim 4M$, it is worth noting that this set of QNMs accurately predicts the remnant quantities with an error of $\sim 10^{-5}$ as early as t_{peak}.

either by extended sourcing of second-order QNMs beyond t_{peak} or by additional unknown nonlinearities. Still, it is reassuring that even without including this unknown content, the set of modes we are fitting with remain an excellent model capable of accurately predicting the remnant quantities at the level of 10^{-4} as early as t_{peak}.

We repeat this same procedure for the case of SXS: BBH:2420, with the results shown in Fig. 9. Here we have included all of the QNMs shown in Fig. 7 while limiting the set of $(2, 2, n)$ modes to $n = \{0, \ldots, N\}$. The values of ϵ at t_{peak} for all N are all smaller than those of SXS:BBH:2423 in Fig. 8. While the floor for ϵ is generally the same for both cases, the ϵ's are smaller at t_{peak} in this case since our model is stable much closer to t_{peak}. The ϵ for $N = 9$ is slightly biased at early times, but reaches its minimum at $\sim 4M$ once the unmodeled content has decayed away. This too is consistent with the time at which we observe stable amplitudes in Fig. 7. So, while we cannot show stable amplitudes for all QNMs before $t = t_{\text{peak}} + 4M$, the model captures the majority of the ringdown signal, precisely predicting the remnant parameters down to a few times 10^{-5} as early as t_{peak}. This is consistent with the result found previously in Ref. [2] for a waveform with similar parameters.

VI. DISCUSSION AND CONCLUSIONS

Understanding the nature of binary black hole ringdowns is critical to future endeavors probing Einstein's general theory of relativity. Whether it is black hole spectroscopy or searching for black hole mimickers, it is essential to understand the physical aspects of ringdown signals. Using some of the highest-accuracy ringdown waveforms available from numerical relativity coupled with a robust nonlinear fitting scheme, we reveal details of the ringdown that were previously unachievable. Through advances in numerical relativity waveform extraction, namely CCE, BMS frame fixing, and removing contributions from the memory, the noise floor in the ringdown of these waveforms is orders of magnitude smaller than those previously available. This, along with the use of variable projection (VARPRO), unveils a number of QNMs in the dominant quadrupolar (2, 2) component of the ringdown that were previously undiscovered. This includes a number of second-order QNMs and overtones of modes present through spherical-spheroidal mixing. In addition to these newly observed modes, we also improve on our ability to numerically extract the many overtones associated with the (2, 2) QNM. Through simplified analytic explorations, we show the high sensitivity of overtones to small amounts of noise and provide an improved method for extending our ability to show stable amplitudes across time.

In the ringdown of a highly spinning remnant, SXS: BBH:2423, we find that the overtones have stable amplitudes over at least $10M$ up to the $n = 7$ overtone, and the next highest two to a lesser extent. Beyond this, we also find four

second-order QNMs, the much sought after nonlinearities that have remained elusive in binary black hole ringdowns. These four QNMs—$\omega_{440} - \omega_{220}^*$, $\omega_{440} - \omega_{320}^*$, $\omega_{220} + \omega_{200}$, and $\omega_{220} - \omega_{200}^*$—turn out to be remarkably stable alongside the many first-order QNMs. While these second-order modes are generally subdominant in amplitude, the loudest of these, $\omega_{440} - \omega_{220}^*$, is likely the best candidate for future observation and may serve as an excellent probe of the nonlinear nature of binary black hole mergers.

In the case of a more typical moderately spinning remnant, SXS:BBH:2420, we find an even greater abundance of modes. Because of the short-lived nature of overtones at lower spins, the highest overtones are shown to be stable over a smaller window of time, while the lower n remain more easily resolvable. In addition to finding more modes from spherical-spheroidal mixing, we find up to the second overtone of the (3, 2) QNM and four more second-order QNMs. These additional second-order QNMs are subdominant to the four found in SXS:BBH:2420, coming from interactions with the (2, 2, 0) and lower amplitude (3, 0, 0) and (4, 0, 0) QNMs. The $\omega_{440} - \omega_{220}^*$ QNM is again the largest amplitude quadratic mode, indicating that this mode likely dominates the second-order QNMs in aligned-spin binary black hole mergers like those considered in this work. Future explorations of more generic systems are necessary to reveal more about the spectrum and excitability of second-order modes in binary ringdowns.

Through this work, we show that with the proper fitting techniques and high-accuracy waveforms we can confidently identify and extract the individual QNMs of the ringdown spectrum. We also confirm the importance of overtones and their physical contribution to binary ringdowns. Further, we show there are indeed nonlinearities in binary black hole ringdowns. One kind of nonlinearity is identifiable second-order QNMs. It is worth emphasizing that, while mathematically these count as a nonlinearity, they are computable by applying linear perturbation theory to second order. In addition, there may perhaps be some still unknown contributions in the early ringdown, with relatively small amplitude.

The second-order QNMs in binary ringdowns will undoubtedly be targets of future detectors probing general relativity. Further studies are necessary to determine the detectability of these modes in future detectors.

DATA AVAILABILITY

The data that support the findings of this article are openly available [39].

APPENDIX A: ALTERNATIVE QNM NOTATIONS

In this paper, we use the notation (ℓ, m, n) to label a QNM, with the convention that the real part of the frequency is always positive. This makes it easy to find numerical values for the QNMs in tables, which typically use this convention. Alternatively, a QNM can be labeled using four indices (ℓ, m, n, p), where its temporal and azimuthal components are explicitly given by

$$e^{-i\omega_{\ell mn}^p t} e^{im\phi}. \tag{A1}$$

The fourth index p can be defined in two different ways:

1. Convention 1

We follow [57] and define $p = \mathrm{sgn}(\mathrm{Re}(\omega)) \times \mathrm{sgn}(m)$. As an example, Fig. 10 shows the real and imaginary parts of QNMs $(\ell = 2, m = \pm 2, n = 0, p = \pm)$ for Kerr BHs parametrized by χ. The four branches correspond to different signs of m and p. The two branches on the left $(p \times \mathrm{sgn}(m) < 0)$ are mirrors of the branches on the right $(p \times \mathrm{sgn}(m) > 0)$. Additionally, a positive p corresponds to a prograde mode while negative p indicates a retrograde mode. The Kerr symmetry yields

$$\omega_{\ell mn}^p = -(\omega_{\ell -mn}^p)^*. \tag{A2}$$

This notation is related to ours via

$$(\ell, m, n) \to \omega_{\ell mn}^+, \qquad -(\ell, m, n)^* \to \omega_{\ell, -m, n}^{\mathrm{sgn}\, m}. \tag{A3}$$

For example, in Fig. 7, the retrograde mode $-(2, -2, 0)^*$ corresponds to $\omega_{2,2,0}^-$. The negative p specifies that it is a retrograde mode, while $p \times m < 0$ indicates that it appears in the negative frequency band. The second order mode $(4, 4, 0) - (2, 2, 0)^*$ represents $\omega_{440}^+ \times \omega_{2,-2,0}^+$, which is generated by two prograde modes. As shown in Fig. 10, $\omega_{2,-2,0}^+$ and ω_{220}^+ are symmetric about the imaginary axis, indicating they are mirrors of each other.
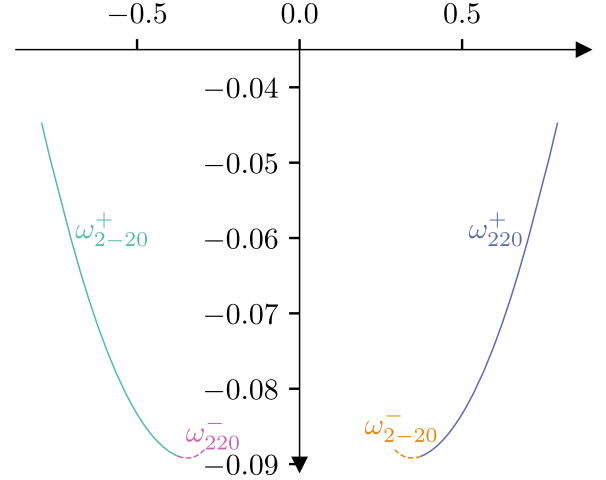

FIG. 10. Four branches of QNMs for Kerr BHs under Convention 1, where $p = \mathrm{sgn}(\mathrm{Re}(\omega)) \times \mathrm{sgn}(m)$. Each curve is parametrized by χ from 0 to 1, with $\chi = 0$ corresponding to the point where the solid and dashed lines meet. The x-axis corresponds to $\mathrm{Re}(\omega)$ and the y-axis to $\mathrm{Im}(\omega)$. Note that pairs of mirror modes are symmetric about the imaginary axis. The prograde modes are denoted by solid lines while the retrograde modes are dashed.

2. Convention 2

Convention 1 has a caveat, as it becomes ambiguous when $m = 0$. One can instead define $p = \mathrm{sgn}(\mathrm{Re}(\omega))$ [17]. In Fig. 11, we explicitly label the four branches of $(\ell = 2, m = \pm 2, n = 0, p = \pm)$ for Kerr BHs, which are again parametrized by χ. In this case, positive p refers to a standard mode and negative p refers to a mirror mode. In this notation, prograde modes satisfy $p \times \mathrm{sgn}(m) > 0$ and retrograde modes have $p \times \mathrm{sgn}(m) < 0$. The Kerr symmetry now yields
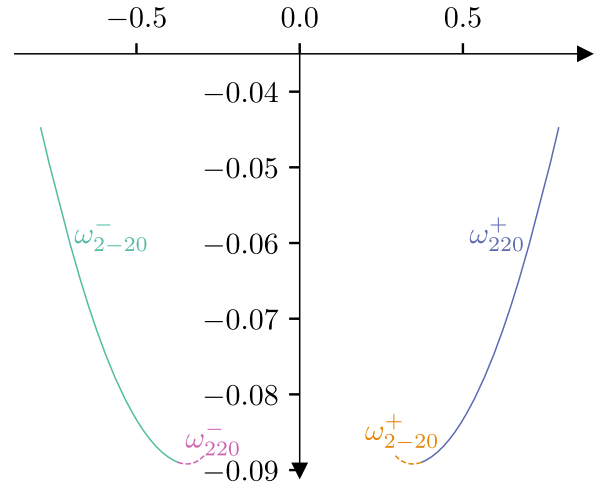

FIG. 11. The four branches of QNMs for Kerr BHs under Convention 2. This is the same as Fig. 10, but with $p = \mathrm{sgn}(\mathrm{Re}(\omega))$.

$$\omega_{\ell mn}^{p} = -(\omega_{\ell -mn}^{-p})^{*}. \qquad (A4)$$

This second notation is related to ours via

$$(\ell, m, n) \rightarrow \omega_{\ell mn}^{+}, \qquad -(\ell, m, n)^{*} \rightarrow \omega_{\ell, -m, n}^{-}. \qquad (A5)$$

For example, in Fig. 7, the second order mode $(2,2,0) - (2,0,0)^{*}$ refers to $\omega_{2,2,0}^{+} \times \omega_{2,0,0}^{-}$, whereas $(2,2,0) + (3,0,0)$ refers to $\omega_{2,2,0}^{+} \times \omega_{3,0,0}^{+}$.

APPENDIX B: EXCITATION FACTORS

The formalism for extracting the QNM contribution to a waveform was first studied in detail by Leaver [26]. Since we are dealing with a linear wave-type equation, the Fourier transform of the solution can be written with a Green's function[5]

$$\Psi_{\ell m}(\omega, r) \sim \int G(r, r', \omega) T(r', \omega) dr'. \qquad (B1)$$

In Eq. (B1) T represents the source term. This could be, for example, the stress-energy from a small particle falling into the black hole. In our case, it is the initial condition for the problem, i.e., the gravitational field outside the black hole at the time we decide to use perturbation theory. The Green's function G can be constructed from the two linearly independent solutions to the homogeneous radial equation.

The solution $\Psi_{\ell m}(t, r)$ in the time domain requires an inverse Fourier transform of Eq. (B1) along a contour in the complex plane (essentially a Laplace transform). The QNM frequencies correspond to the poles of G in the complex plane, with n labeling the poles in order of increasing imaginary part. The contribution of G to the solution (B1) will include a sum over the residues $E_{\ell mn}$ at these poles. So the mode amplitudes $C_{\ell mn}$ will be a product of two factors,

$$C_{\ell mn} = E_{\ell mn} T_{\ell mn}, \qquad (B2)$$

where the $T_{\ell mn}$ come from the radial integral in Eq. (B1) and depend explicitly on the source of the perturbation.

Now comes a key point: If the source factors $T_{\ell mn}$ are slowly varying with n, then the mode amplitudes $C_{\ell mn}$ will be nearly proportional to $E_{\ell mn}$. Since the $E_{\ell mn}$ come from the homogeneous solutions to the perturbation equation, they are universal constants that depend only on M and χ—the mass and dimensionless spin of the remnant black hole—and are called excitation factors.

There have been several advances in the calculation of excitation factors since the work of Leaver [26,59–62]. Most relevant for us is the work of Oshita [62], who showed

---

[5]See Sec.§7.3 in Ref. [58]. A pedagogical example is in Ref. [59].

that the assumption that the $T_{\ell mn}$ do not vary much does appear to be valid for black hole mergers, at least for the low values of n that we are interested in.

In light of this, along with the difficulties in individually resolving the $n = 5$ mode in previous work, one proposed method to determine the presence of this mode is to fit for the amplitudes of all n and compare the structure of the measured amplitudes to the structure of the excitation factors. In the work of Oshita [62], the $n = 5$ excitation factor begins rapidly decreasing with respect to the other n beyond $\chi \sim 0.9$. This peculiar feature in the excitability of the modes suggests that the $n = 5$ mode should have a reduced amplitude at higher spins, creating a unique signature in the structure of the mode amplitudes. So, if we look at the amplitudes of the modes as a function of n, a dip should be expected in the amplitude of the $n = 5$ mode once the remnant spin is sufficiently high. If the measured C_{22n} agree well with the known E_{22n}, this indicates that the fit is sensitive to each n within the ringdown.

But, before we consider this unique feature of highly spinning remnants, it is useful to first consider how well the excitation factors E_{22n} agree with the measured NR amplitudes C_{22n} in the moderate-spin case considered in this work. The excitation factors described in Oshita [62] are defined and computed with respect to the strain. Since the NR amplitudes are obtained from fits to the news, the first derivative of the strain, we instead compare the measured C_{22n} to $\omega_{22n} E_{22n}$. Another important aspect in comparing the NR amplitudes to the excitation factors of Oshita [62] is a quantity t_0 that defines the start of the ringdown and appears in the equations for the excitation factors. Since the connection between this t_0 and the NR time coordinate is not well understood, we simply choose a value of t_0 that produces reasonable agreement between the amplitudes and the excitation factors. The final freedom in comparing the excitation factors to measured amplitudes is an overall scale factor, since the measured amplitudes are a product of the excitation factors and a source term, $E_{22n} T_{22n}$. Although the source contribution is n-dependent, for simplicity, we apply the same scale factor across all n by normalizing both the measured amplitudes and the excitation factors such that $C_{220} = \omega_{220} E_{220} = 1$. In Fig. 12, we show a comparison between the NR amplitudes C_{22n} measured in the ringdown of SXS:BBH:2420 from Sec. V C and the $\omega_{22n} E_{22n}$ associated with $\chi = 0.75$, the spin of the SXS:BBH:2420 remnant. In Fig. 12, the excitation factors are computed using a value of $t_0 = 2.5M$, while the NR values correspond to those measured at $4M$ after the peak of the $(2, 2)$ component of the strain. Overall, Fig. 12, shows that the measured NR amplitudes and the excitation factors associated with the NR remnant are in good agreement across all n.

Returning to the case of a highly spinning remnant, we now consider how well the excitation factors agree with the measured NR amplitudes in the domain where $n = 5$
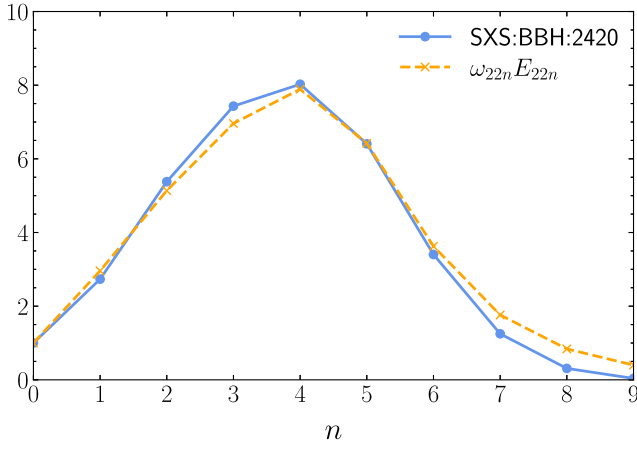
FIG. 12. The $(2, 2, n)$ NR amplitudes as measured in the moderate-spin case of SXS:BBH:2420 and the excitation factors $\omega_{22n}E_{22n}$ for $\chi = 0.75$. The excitation factors are computed using $t_0 = 2.5$ and both curves are normalized such that $C_{220} = \omega_{220}E_{220} = 1$.

begins to behave peculiarly. In Fig. 13, we compare the NR amplitudes C_{22n} measured in the ringdown of SXS:BBH:2423 from Sec. V A and the $\omega_{22n}E_{22n}$ associated with $\chi = 0.92$, the spin of the SXS:BBH:2423 remnant. The excitation factors and measured amplitudes are, again, both normalized. The NR amplitudes correspond to those measured at $8M$ after the peak of the $(2, 2)$ component of the strain and a value of $t_0 = 0.9$ is used to compute the excitation factors. In this case, Fig. 13 shows excellent agreement for $n < 5$, good structural agreement for $n > 5$, while $n = 5$ noticeably differs. While the structure of the amplitudes in this case shows the characteristic dip in the $n = 5$ amplitude, the excitation factors do not predict a dip of this magnitude until χ is a bit larger. So in this particular case, there is apparent disagreement between the $n = 5$ excitation factor and the NR amplitude. In the case of SXS:
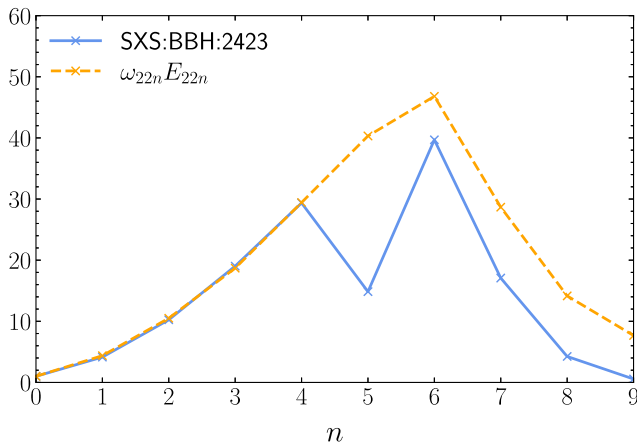

FIG. 13. The $(2, 2, n)$ NR amplitudes as measured in the high-spin case of SXS:BBH:2423 and the excitation factors $\omega_{22n}E_{22n}$ for $\chi = 0.92$. The excitation factors are computed using $t_0 = 0.9$ and both curves are normalized such that $C_{220} = \omega_{220}E_{220} = 1$.

BBH:2423, with a remnant spin of $\chi = 0.92$, the behavior, in particular the frequency, of the $n = 5$ mode has already deviated from the general trend that the other n follow as a function of χ. As can be seen in Fig. 14, whereas all $n \neq 5$ modes generally converge in the real part of the frequency as $\chi \to 1$, $n = 5$ becomes an outlier and remains at a much lower frequency than the other n. Given that the source terms are effectively overlap integrals with the QNM eigenfunctions, we speculate that the anomalous behavior of the $n = 5$ mode leads to anomalous sourcing. Consequently, the $n = 5$ is sourced to a lesser extent than the other n.

Note that it is possible to choose to normalize the excitation factors by an arbitrary constant scale factor, rather than by the value for $n = 0$. This normalization factor can be used to improve the agreement with the $n = 5$ dip in Fig. 13 somewhat. However, the agreement with the other values of n becomes worse.

Overall, we find that the amplitudes measured in the ringdowns of NR waveforms are generally in good agreement with the excitation factors determined purely by M and χ. Although the proposal of comparing amplitudes to excitation factors as proof of a particular mode measurement is interesting in theory, more work is necessary to better understand the source factor contributions to mode amplitudes. Given this, we leave a more rigorous investigation of the relation between excitation factors and QNM amplitudes to future work and instead rely on our time-dependent measurement in Fig. 6 of Sec. V B as evidence for the presence of the anomalous $n = 5$ mode.
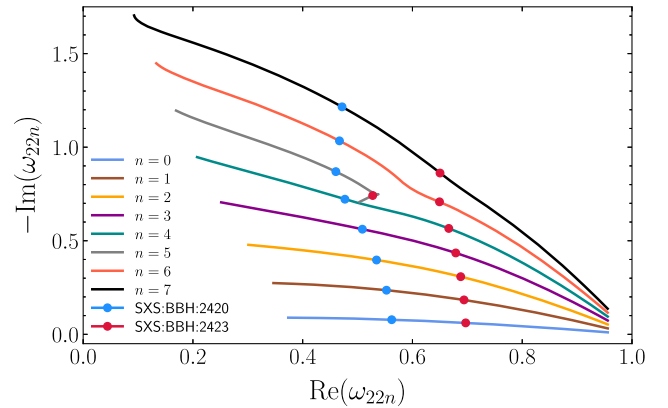

FIG. 14. The $(2, 2, n)$ frequencies up to $n = 7$ parametrized by χ from 0 to 1, with $\chi = 0$ corresponding to the leftmost point of each curve. Notice that all the curves, except for $n = 5$, converge toward the same point as $\chi \to 1$. This divergence from the trend for $n = 5$, with a peculiar turnaround at $\chi \sim 0.9$, is why the $n = 5$ mode is often deemed anomalous. The blue dots are the QNMs associated with $\chi = 0.76$, the remnant spin in SXS:BBH:2420, and the red dots are those for $\chi = 0.92$, the remnant spin in SXS:BBH:2423. Notice that in the higher spin case the $n = 5$ mode becomes an outlier, remaining at a much lower frequency than the other n, whereas in the lower spin case the mode frequencies are more generally aligned.

[1] S. A. Teukolsky, Perturbations of a rotating black hole. 1. Fundamental equations for gravitational electromagnetic and neutrino field perturbations, Astrophys. J. **185**, 635 (1973).

[2] M. Giesler, M. Isi, M. A. Scheel, and S. Teukolsky, Black hole ringdown: The importance of overtones, Phys. Rev. X **9**, 041060 (2019).

[3] P. Mourier, X. Jiménez Forteza, D. Pook-Kolb, B. Krishnan, and E. Schnetter, Quasinormal modes and their overtones at the common horizon in a binary black hole merger, Phys. Rev. D **103**, 044054 (2021).

[4] J. L. Jaramillo, R. Panosso Macedo, and L. Al Sheikh, Pseudospectrum and black hole quasinormal mode instability, Phys. Rev. X **11**, 031003 (2021).

[5] X. J. Forteza and P. Mourier, High-overtone fits to numerical relativity ringdowns: Beyond the dismissed $n = 8$ special tone, Phys. Rev. D **104**, 124072 (2021).

[6] V. Baibhav, M. H.-Y. Cheung, E. Berti, V. Cardoso, G. Carullo, R. Cotesta, W. Del Pozzo, and F. Duque, Agnostic black hole spectroscopy: Quasinormal mode content of numerical relativity waveforms and limits of validity of linear perturbation theory, Phys. Rev. D **108**, 104020 (2023).

[7] M. H.-Y. Cheung, E. Berti, V. Baibhav, and R. Cotesta, Extracting linear and nonlinear quasinormal modes from black hole merger simulations, Phys. Rev. D **109**, 044069 (2024).

[8] H. Zhu, J. L. Ripley, A. Cárdenas-Avendaño, and F. Pretorius, Challenges in quasinormal mode extraction: Perspectives from numerical solutions to the Teukolsky equation, Phys. Rev. D **109**, 044010 (2024).

[9] P. J. Nee, S. H. Völkel, and H. P. Pfeiffer, Role of black hole quasinormal mode overtones for ringdown analysis, Phys. Rev. D **108**, 044032 (2023).

[10] L. London, D. Shoemaker, and J. Healy, Modeling ringdown: Beyond the fundamental quasinormal modes, Phys. Rev. D **90**, 124032 (2014); **94**, 069902(E) (2016).

[11] K. Mitman *et al.*, Nonlinearities in black hole ringdowns, Phys. Rev. Lett. **130**, 081402 (2023).

[12] M. H.-Y. Cheung *et al.*, Nonlinear effects in black hole ringdown, Phys. Rev. Lett. **130**, 081401 (2023).

[13] S. Ma, K. Mitman, L. Sun, N. Deppe, F. Hébert, L. E. Kidder, J. Moxon, W. Throwe, N. L. Vu, and Y. Chen, Quasinormal-mode filters: A new approach to analyze the gravitational-wave ringdown of binary black-hole mergers, Phys. Rev. D **106**, 084036 (2022).

[14] J. Moxon, M. A. Scheel, and S. A. Teukolsky, Improved Cauchy-characteristic evolution system for high-precision numerical relativity waveforms, Phys. Rev. D **102**, 044052 (2020).

[15] J. Moxon, M. A. Scheel, S. A. Teukolsky, N. Deppe, N. Fischer, F. Hébert, L. E. Kidder, and W. Throwe, SPECTRE Cauchy-characteristic evolution system for rapid, precise waveform extraction, Phys. Rev. D **107**, 064013 (2023).

[16] N. Deppe *et al.*, SPECTRE v2025.03.17 Zenodo (2023), 10.5281/zenodo.15040490.

[17] L. Magaña Zertuche *et al.*, High precision ringdown modeling: Multimode fits and BMS frames, Phys. Rev. D **105**, 104015 (2022).

[18] K. Mitman *et al.*, A review of gravitational memory and BMS frame fixing in numerical relativity, Classical Quantum Gravity **41**, 223001 (2024).

[19] K. Mitman *et al.*, Fixing the BMS frame of numerical relativity waveforms, Phys. Rev. D **104**, 024051 (2021).

[20] K. Mitman *et al.*, Fixing the BMS frame of numerical relativity waveforms with BMS charges, Phys. Rev. D **106**, 084029 (2022).

[21] M. Boyle, Transformations of asymptotic gravitational-wave data, Phys. Rev. D **93**, 084031 (2016).

[22] D. A. B. Iozzo *et al.*, Comparing remnant properties from horizon data and asymptotic data in numerical relativity, Phys. Rev. D **103**, 124029 (2021).

[23] O. M. Moreschi, Supercenter of mass system at future null infinity, Classical Quantum Gravity **5**, 423 (1988).

[24] O. M. Moreschi and S. Dain, Rest frame system for asymptotically flat space-times, J. Math. Phys. (N.Y.) **39**, 6631 (1998).

[25] S. Dain and O. M. Moreschi, General existence proof for rest frame systems in asymptotically flat space-time, Classical Quantum Gravity **17**, 3663 (2000).

[26] E. W. Leaver, Spectral decomposition of the perturbation response of the Schwarzschild geometry, Phys. Rev. D **34**, 384 (1986).

[27] H.-P. Nollert, TOPICAL REVIEW: Quasinormal modes: The characteristic "sound" of black holes and neutron stars, Classical Quantum Gravity **16**, R159 (1999).

[28] N. Andersson, Evolving test fields in a black hole geometry, Phys. Rev. D **55**, 468 (1997).

[29] A. Chavda, M. Lagos, and L. Hui, The impact of initial conditions on quasi-normal modes, arXiv:2412.03435.

[30] H. Zhu *et al.*, Imprints of changing mass and spin on black hole ringdown, Phys. Rev. D **110**, 124028 (2024).

[31] T. May, S. Ma, J. L. Ripley, and W. E. East, Nonlinear effect of absorption on the ringdown of a spinning black hole, Phys. Rev. D **110**, 084034 (2024).

[32] S. A. Teukolsky, Rotating black holes—separable wave equations for gravitational and electromagnetic perturbations, Phys. Rev. Lett. **29**, 1114 (1972).

[33] W. H. Press and S. A. Teukolsky, Perturbations of a rotating black hole. II. Dynamical stability of the Kerr metric, Astrophys. J. **185**, 649 (1973).

[34] C. Lanczos, *Applied Analysis* (Prentice-Hall, Englewood Cliffs, NJ, 1956), §4.23.

[35] G. H. Golub and V. Pereyra, The differentiation of pseudo-inverses and nonlinear least squares problems whose variables separate, SIAM J. Numer. Anal. **10**, 413 (1973).

[36] G. H. Golub and V. Pereyra, The differentiation of pseudo-inverses and nonlinear least squares problems whose variables separate, Technical Report STAN-CS-72-261, Computer Science Department, Stanford University, Stanford, CA, 1972.

[37] D. P. O'Leary and B. W. Rust, Variable projection for nonlinear least squares problems, Comput. Optim. Applic. **54**, 579 (2013).

[38] https://github.com/sxs-collaboration/varpro

[39] M. Giesler *et al.*, Overtones and nonlinearities in binary black hole ringdowns—waveform data, 10.5281/zenodo.15086488 (2025).

[40] https://www.black-holes.org/code/SpEC.html

[41] M. Boyle, D. Iozzo, L. Stein, A. Khairnar, H. Rüter, M. Scheel, V. Varma, and K. Mitman, SCRI (2024), 10.5281/zenodo.4041971.

[42] M. Boyle, Angular velocity of gravitational radiation from precessing binaries and the corotating frame, Phys. Rev. D **87,** 104006 (2013).

[43] M. Boyle, L. E. Kidder, S. Ossokine, and H. P. Pfeiffer, Gravitational-wave modes from precessing black-hole binaries, arXiv:1409.4431.

[44] K. Mitman *et al.*, Adding gravitational memory to waveform catalogs using BMS balance laws, Phys. Rev. D **103,** 024031 (2021).

[45] R. Geroch, Asymptotic structure of space-time, in *Symposium on Asymptotic Structure of Space-Time* (Springer US, Boston, MA, 1977), 10.1007/978-1-4684-2343-3_1.

[46] A. Ashtekar and M. Streubel, Symplectic geometry of radiative modes and conserved quantities at null infinity, Proc. R. Soc. A **376,** 585 (1981).

[47] A. Ashtekar, T. De Lorenzo, and N. Khera, Compact binary coalescences: Constraints on waveforms, Gen. Relativ. Gravit. **52,** 107 (2020).

[48] Y. B. Zel'dovich and A. G. Polnarev, Radiation of gravitational waves by a cluster of superdense stars, Sov. Astron. **18,** 17 (1974), https://ui.adsabs.harvard.edu/abs/1974SvA...18...17Z.

[49] V. B. Braginsky and L. P. Grishchuk, Kinematic resonance and memory effect in free mass gravitational antennas, Sov. Phys. JETP **62,** 427 (1985), https://ui.adsabs.harvard.edu/abs/1985JETP...62..427B.

[50] V. B. Braginsky and K. S. Thorne, Gravitational-wave bursts with memory and experimental prospects, Nature (London) **327,** 123 (1987).

[51] P. N. Payne, Smarr's zero frequency limit calculation, Phys. Rev. D **28,** 1894 (1983).

[52] D. Christodoulou, Nonlinear nature of gravitation and gravitational wave experiments, Phys. Rev. Lett. **67,** 1486 (1991).

[53] L. Blanchet and T. Damour, Hereditary effects in gravitational radiation, Phys. Rev. D **46,** 4304 (1992).

[54] K. S. Thorne, Gravitational-wave bursts with memory: The Christodoulou effect, Phys. Rev. D **45,** 520 (1992).

[55] E. E. Flanagan and D. A. Nichols, Conserved charges of the extended Bondi-Metzner-Sachs algebra, Phys. Rev. D **95,** 044002 (2017); **108,** 069902(E) (2023).

[56] K. Mitman, J. Moxon, M. A. Scheel, S. A. Teukolsky, M. Boyle, N. Deppe, L. E. Kidder, and W. Throwe, Computation of displacement and spin gravitational memory in numerical relativity, Phys. Rev. D **102,** 104007 (2020).

[57] M. Isi and W. M. Farr, Analyzing black-hole ringdowns, arXiv:2107.05609.

[58] P. M. Morse and H. Feshbach, *Methods of Theoretical Physics* (McGraw-Hill, New York, 1953).

[59] E. Berti and V. Cardoso, Quasinormal ringing of Kerr black holes. I. The excitation factors, Phys. Rev. D **74,** 104020 (2006).

[60] K. Glampedakis and N. Andersson, Quick and dirty methods for studying black hole resonances, Classical Quantum Gravity **20,** 3441 (2003).

[61] Z. Zhang, E. Berti, and V. Cardoso, Quasinormal ringing of Kerr black holes. II. Excitation by particles falling radially with arbitrary energy, Phys. Rev. D **88,** 044018 (2013).

[62] N. Oshita, Ease of excitation of black hole ringing: Quantifying the importance of overtones by the excitation factors, Phys. Rev. D **104,** 124032 (2021).